EIGHTH EUROPEAN ROTORCRAFT FORUM

Paper No. 3.11

ON THE ADEQUACY OF MODELING DYNAMIC INFLOW FOR HELICOPTER FLAP-LAG STABILITY

G.H. GAONKAR, V.V.S.S. SASTRY, T.S.R. REDDY

Indian Institute of Science

Bangalore, India

D.A. PETERS

Washington University

St. Louis, Missouri, U.S.A. 63130

August 31 through September 3, 1982

AIX-EN-PROVENCE, FRANCE

ASSOCIATION AERONAUTIQUE ET ASTRONAUTIQUE DE FRANCE

ON THE ADEQUACY OF MODELING DYNAMIC INFLOW FOR HELICOPTER FLAP-LAG STABILITY

G.H. Gaonkar, V.V.S.S. Sastry, T.S.R. Reddy
Indian Institute of Science
Bangalore, India

D.A. Peters
Washington University
St. Louis, Missouri, USA

ABSTRACT

A hierarchy of thirteen unsteady and quasisteady inflow models is generated for predicting flap-lag damping in hovering and forward flight. It comprises the development of 5×5 inflow-gain matrices in analytic form from available numerical data. It is based on a time-delayed, unsteady momentum theory according to a first-order harmonic description of inflow and on an unsteady actuator-disk theory according to both first and second-order harmonic descriptions of inflow. In the absence of test data, the analytical model from the unsteady actuator-disk theory with a second-order harmonic representation is taken as a base-line model for comparative purposes only. For typical flight regimes (advance ratio $.2 < \mu < .4$), the quasisteady treatment of a simplified actuator-disk model adequately predicts lag regressing and collective mode damping, albeit several unexpected subtleties do occur.

NOMENCLATURE

a	Lift curve slope, rad^{-1}
$[A(t)], B(t), [F(t)]$ $[C(t)], [N(t)][G(t)]$	Typical state, multiblade transformation and coupling matrices, periodic with 2π
C_L	Harmonic perturbation of roll-moment coefficient (roll moment/$\rho\pi\Omega^2R^5$), positive advancing blade down
C_M	Harmonic perturbation of pitch-moment coefficient (pitch moment/$\rho\pi\Omega^2R^5$), positive nose-up
C_{2L}, C_{2M}	Second-harmonic pressure perturbation coefficients for roll and pitch
C_T	Harmonic perturbation of thrust coefficient (also steady thrust coefficient ($T/\rho\pi\Omega^2R^4$) in eqn. (9) and figures)
c_d, c_d^*	Profile drag coefficient, equivalent profile drag coefficient
$\bar{f}$	Dimensionless helicopter flat plate area
$\bar{F}_\beta$	Dimensionless force per unit length, perpendicular to blade and direction of rotation
$\{F\}$	Harmonics of disc loading
L	Lift on actuator disc

$[L],[M]$	Dynamic inflow and apparent mass matrices
N	Number of blades or coupling matrix
P	Dimensionless rotating flap frequency
r	Radial distance/Rotor radius R
T	Rotor thrust
t	Dimensionless time (identical with blade azimuth position of first blade, ψ_1)
U,X,Y	Typical state vectors
$\{V\}$	Inflow vector
v	Flow rate parameter
W	Lead-lag stiffness
Z	Flap-lag coupling
α	Wake skew angle
α_s	Rotor shaft angle, positive nose down
β	Perturbation flapping angle
$\beta_o(\zeta_o),\beta_s(\zeta_s)$ and $\beta_c(\zeta_c)$	Multiblade flapping (lead-lag) coordinates: Coning, and first order cyclic flapping (lead-lag) components
$\bar{\beta}$	Equilibrium flapping angle = $\bar{\beta}_o + \bar{\beta}_s \sin\psi + \bar{\beta}_c \cos\psi$
γ,γ^*	Lock number, equivalent Lock number
η	Damping or real portion of characteristic exponents
σ	Rotor solidity
$\bar{\lambda}$	Steady inflow (free-stream plus induced flow)
μ	Rotor advance ratio
ν	Inflow perturbation
$\nu_o,\nu_s,\nu_c,\nu_{2s}$, and ν_{2c}	Components of inflow perturbations
$\bar{\nu}$	Induced flow due to steady rotor thrust
ψ_k	Azimuth position of the k-th blade (identical with t_k), $\psi_k = (\frac{2\pi}{N})(k-1) + t$
ψ	Spacial azimuth position
ω_ζ	Dimensionless inplane frequency
$(\cdot)$	d/dt

1. Introduction

Dynamic inflow refers to the low-frequency properties of the rotor wake under unsteady conditions.[1-3] It does not comprise conventional unsteady airfoil aerodynamics which is usually applied to high-frequency phenomena such as flutter.[1-3] Given the wake complexity, even for steady flight conditions, a thorough and yet tractable treatment of the complete wake is unlikely for flight dynamics applications.[1-3] Therefore it is often treated approximately on the basis of a momentum theory (a time-delayed unsteady momentum theory)[2-4] or a potential theory (an unsteady actuator-disk theory).[5] Irrespective of the theoretical basis, dynamic inflow at a point in the rotor disk is assumed to have a first[1-4] or second-order harmonic representation[5] in terms of inflow distributions (uniform, fore-to-aft etc.).[2-5] These distributions assume the role of degrees of freedom. They are related to perturbations in rotor air loads by linear, first-order models involving only matrices of inflow gain and time constants[1-5] (i.e. the L and diagonal M matrices). The quasisteady formulation, in which the effects of apparent inflow mass are neglected, provides a means of accounting for inflow without increasing the system dimension. With momentum theory as a basis and with the axial flow (e.g. hovering) approximation, quasisteady theory leads to the method of equivalent Lock number γ^* and drag coefficient c_d^*.[4,6-8]

This means, before we come to the question of adequacy of an inflow model with minimum degrees of freedom, a hierarchy of unsteady and quasisteady models, including the method of 'γ^* - c_d^*',[4,6-8] must be generated. The hierarchy of inflow models to be considered in this research is outlined in Figure 1. Each formulation is classified according to its analytical basis (momentum theory or potential theory) and according to the assumed inflow descriptions (first and second-order harmonic representations that lead to three and five degrees of freedom, respectively). The justification of these various inflow models is as follows. In hovering, unsteady momentum theory with three degrees of freedom provides forced-response results[2,9] and transient-response results[7,10,11] that correlate with measured test data. However, in forward flight, momentum theory gives less than adequate correlation with test data[2,11]. Despite the inadequacies of momentum theory, and in the absence of a viable alternative, it has been used in the analysis of flap[2] and flap-lag instabilities[10,11] as well as in conjunction with the parameter identification of rotor-inflow systems.[10,11] Although other possibilities have been pursued, such as a simple vortex model[5,12] and an empirical model,[2,4] until recently none of these have been a satisfactory replacement for momentum theory.[5] The recent development that may change this, however, is the introduction of an unsteady inflow model based on potential flow theory.[5,13] This inflow model is derived from first principles and is very promising, although it has not yet been applied to rotor or flight-dynamics problems. Furthermore, the model has several possible formulations (based on number of harmonics, radial distribution, or unsteady versus quasi-steady) that likewise have not been applied to rotor dynamics, but which are utilized in the inflow hierarchy to be studied here, Figure 1.

The crux of the problem then boils down to the adequacy of each inflow model in this hierarchy, rather than to the development or use of a particular inflow model on an ad hoc basis. The question naturally arises as to how to assess this adequacy. In other words, "how sophisticated an inflow model is needed?" With emphasis on non-axial flow conditions (e.g. forward flight), we attempt to present such an assessment for predicting damping levels of multiblade flap and inplane modes ('flap-lag damping' for short).

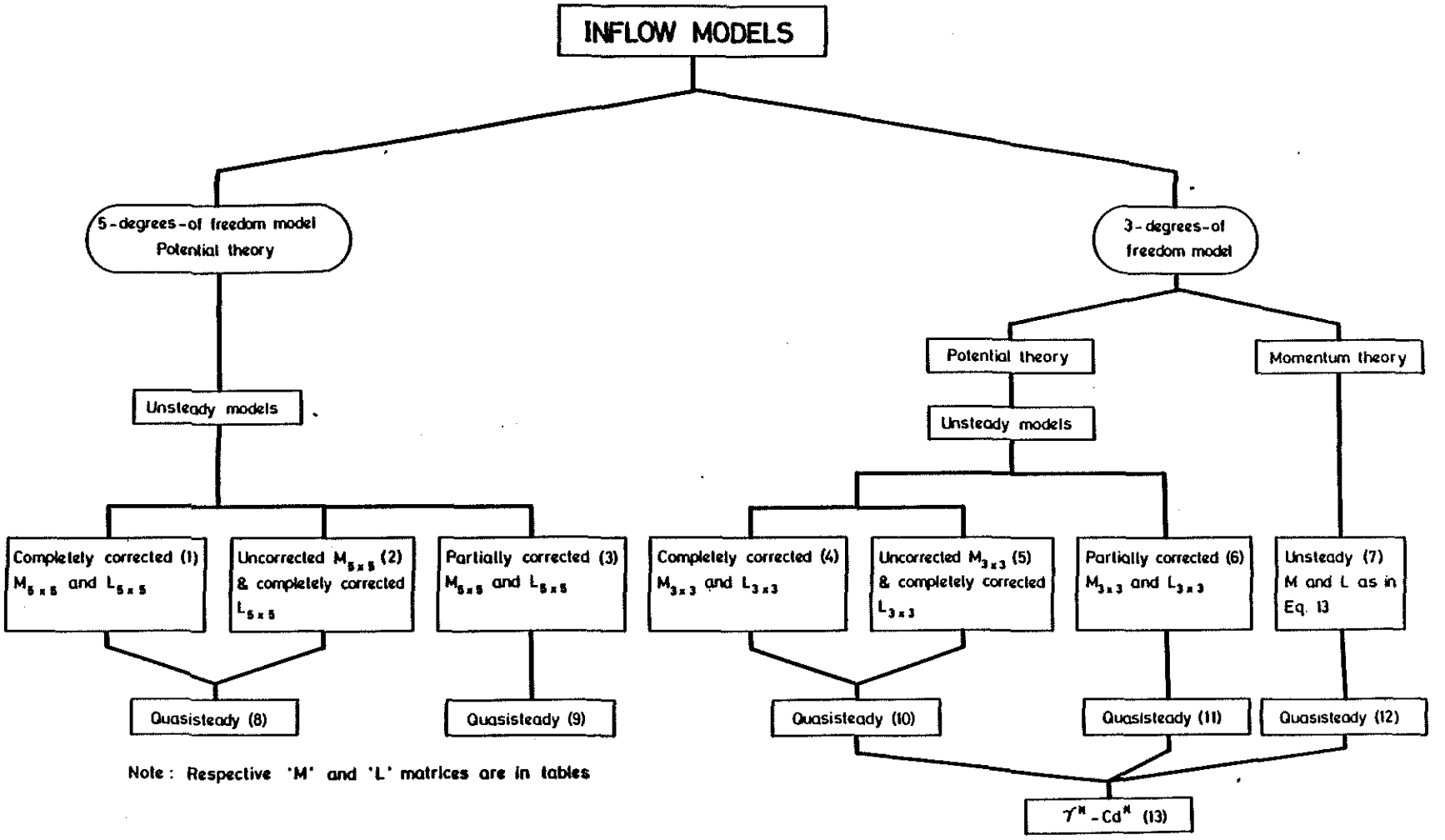

Fig. 1. HIERARCHY OF THIRTEEN INFLOW MODELS.

2. Dynamic Inflow Models

Here, we introduce the dynamic inflow models in detail. They are based on both momentum theory[2,4,8] and potential theory,[5,13] including the corresponding quasisteady approximations and the $\gamma^* - c_d^*$ formulation.[4,6-8] The dynamic inflow ν is perturbed with respect to the steady inflow $\bar{\lambda}$ such that the total induced flow λ is given by

$$\lambda = \bar{\lambda} + \nu \tag{1}$$

where $\bar{\lambda}$ is the average inflow. At any point on the rotor disc (r,ψ), the dynamic perturbations in induced flow are approximated by a truncated Fourier series with prescribed radial distributions.

$$\nu = \nu_o + \nu_s r\sin\psi + \nu_c r\cos\psi + \nu_{2s} r^2\sin 2\psi + \nu_{2c} r^2\cos 2\psi \tag{2}$$

The component ν_o in equation (2) is a uniform component, ν_s and ν_c are side-to-side and fore-to-aft variations, and ν_{2s} and ν_{2c} are higher-harmonic variations. The coefficients in equation (2) are unspecified functions of time and are taken as a state vector, $\{V_5\}$

$$\{V_5\}_{5\times 1} = \begin{Bmatrix} \nu_o \\ \nu_s \\ \nu_c \\ \nu_{2s} \\ \nu_{2c} \end{Bmatrix} = \begin{Bmatrix} \{V_3\}_{3\times 1} \\ \nu_{2s} \\ \nu_{2c} \end{Bmatrix} = \begin{Bmatrix} \{V_1\}_{1\times 1} \\ \nu_s \\ \nu_c \\ \nu_{2s} \\ \nu_{2c} \end{Bmatrix} \tag{3}$$

Further truncations, $\{V_3\}$ and $\{V_1\}$, are defined by elimination of (ν_{2s},ν_{2c}) and (ν_s,ν_c), respectively.

The elements of $\{V\}$, in dynamic inflow theory, are assumed to be linearly related to the harmonics of the disc loading on the rotor. In other words, potential flow theory and momentum theory assume an actuator disc across which is a pressure drop that varies continuously with radius and azimuth (i.e. an infinite number of blades). For rotors with a finite number of blades, however, blade loading rather than disc loading must be defined. Therefore, we approximate the disc-loading harmonics by the following instantaneous functions of the blade loading, $\bar{F}_\beta$.

$$C_T = + \frac{a\sigma}{\gamma N}\cos\beta \sum_{k=1}^{N}\left(\int_0^1 (\bar{F}_\beta)_k\, dx\right) \tag{4b}$$

$$C_L = - \frac{a\sigma}{\gamma N}\cdot \sum_{k=1}^{N}\left(\int_0^1 (\bar{F}_\beta)_k x\, dx\right) \sin\psi_k \tag{4c}$$

$$C_M = - \frac{a\sigma}{\gamma N} \sum_{k=1}^{N}\left(\int_0^1 (\bar{F}_\beta)_k x\, dx\right) \cos\psi_k \tag{4d}$$

$$C_{2L} = -\frac{a\sigma}{\gamma N}\sum_{k=1}^{N}\left(\int_0^1 (\bar{F}_\beta)_k x^2\,dx\right)\sin 2\psi_k \tag{4e}$$

$$C_{2M} = -\frac{a\sigma}{\gamma N}\sum_{k=1}^{N}\left(\int_0^1 (\bar{F}_\beta)_k x^2\,dx\right)\cos 2\psi_k \tag{4f}$$

These loadings are also placed in vector form, $\{F_5\}$

$$\{F_5\}_{5\times 1} = \begin{Bmatrix} C_T \\ C_L \\ C_M \\ C_{2L} \\ C_{2M} \end{Bmatrix} = \begin{Bmatrix} \{F_3\}_{3\times 1} \\ C_{2L} \\ C_{2M} \end{Bmatrix} = \begin{Bmatrix} \{F_1\}_{1\times 1} \\ C_L \\ C_M \\ C_{2L} \\ C_{2M} \end{Bmatrix} \tag{5}$$

with correspondingly truncated versions $\{F_3\}$ and $\{F_1\}$.

The relationship between the inflow harmonics $\{V\}$ and the loading harmonics $\{F\}$ is given in dynamic inflow theory by first-order equations in either of the following forms

$$[m]\{\dot{V}\} + [L]^{-1}\{V\} = \{F\} \tag{6a}$$

$$[L][m]\{\dot{V}\} + \{V\} = [L]\{F\} \tag{6b}$$

where [m] and [L] may assume 5×5 forms, 3×3 forms, or even 1×1 forms depending upon the choice for $\{V\}$ and $\{F\}$. In the truncated version, it is the truncated [L] matrix that is to be inverted in equation (6a); one should <u>not</u> truncate the inverted matrix $[L_5]^{-1}$. (The former implies a constraint on higher inflow harmonics whereas the latter implies the less physical concept of constraining higher-harmonic loads.)

The various inflow models discussed in this paper may be thought of as different expressions for the [L] and [M] matrices of equation (6). For example, the classical momentum theory of references 2 and 4 may be defined by diagonal matrices for $[L_3]$ and $[M_3]$,

$$m_{11} = \frac{8}{3\pi}\,,\quad m_{22} = m_{33} = -\frac{16}{45\pi} \tag{7a}$$

$$L_{11} = \frac{1}{2v}\,,\quad L_{22} = L_{33} = -2/v \tag{7b}$$

where the inflow parameter v is given by

$$v = \frac{\mu^2 + \bar{\lambda}(\bar{\lambda}+\bar{v})}{\sqrt{\mu^2+\bar{\lambda}^2}} \tag{7c}$$

Other inflow models used here are primarily based on the actuator-disc theory of references 5, 13, and 14. From that theory, several alternative versions of [L] and [M] are given. Two of the alternative [M]-matrices, labelled

"corrected" and "uncorrected," are given in Table 1. A third version of [M], "partially corrected," is formed by setting $M_{11} = 128/75\pi$ in the uncorrected version of Table 1. In a similar manner, corrected and partially corrected [L] matrices are used, as given in Table 2. (An uncorrected [L] matrix is also defined in Reference 13 but is not used here.)

The physical significance of "corrected" and "uncorrected" is as follows. In the uncorrected results, the radial distribution of lift is taken to be the simplest possible distribution that is allowed within the framework of actuator-disc theory. In the corrected results, extra terms are added to the formulation of rotor lift in order to enforce special boundary conditions at the rotor center. For rotor thrust, C_T, the uncorrected distribution has finite lift at $r = 0$ whereas the corrected distribution has zero lift at $r = 0$. For moments, C_L and C_M, even the uncorrected distribution has zero lift at the center; but the corrected distribution has, in addition, that the derivative of lift (with respect to r) is zero at the center. For second moments, the "corrected" and "uncorrected" models are identical to each other; and they satisfy both $L = 0$ and $dL/dr = 0$ at the center. From the above definitions, we see that the corrected thrust distribution is physically more reasonable than the uncorrected, because a rotor cannot develop lift at the hub. On the other hand, the corrected moment distributions are no more reasonable than are the uncorrected distributions. The two models merely provide a range of possibilities. Because of this, a third type of [L] or [M] matrix is defined in reference 13 with a corrected first column (to give more accurate thrust) but with uncorrected second and third columns (to capitalize on the simplicity and symmetry of the uncorrected model). This third model is what we have defined in Tables 1 and 2 as "partially corrected." It is interesting to note that the elements of [L] in Table 2 vary continuously with α from 0° (edgewise flow) to 90° (axial flow), and they agree exactly with momentum theory in the latter case. Another interesting aspect of Table 2 is that all elements of the corrected and uncorrected [L] matrices have been assigned closed-form, analytic expressions. This is not the case in previous work, in which some elements are given by numerical plots only. Here, we have been able to develop accurate, closed-form expressions by judicious combinations of base functions in order to fit the numerical data.[5,13,14] We also note that closed-form values for the corrected L_{22} and L_{13} elements at $\alpha = 0°$ are incorrect in reference 5, but are correct here and in reference 13.

All in all, a hierarchy of thirteen inflow models is used, as shown in Figure 1. By stipulation, model no. 1 is the reference or base line model. A scheme of assessing the adequacy of different inflow models is outlined in Figure 2. Its raison d'etre and basic aspects are delineated below:

1. The reference model is based on a rigorous potential theory with a second harmonic inflow distribution. Given the spatially-averaged nature of dynamic inflow, Fourier representation beyond the second harmonic is not required.[5,12,13] In the absence of test data on flap-lag damping, model no. 1 provides a natural base-line model for comparing different inflow models, although it is not necessarily the "best" model.

2. This hierarchy includes seven typical unsteady models including the momentum theory model (no. 7 in figure 1) and model no. 6, which is recommended recently[5,13] as being "probably adequate for rotary-wing dynamics".[5,13] According to reference 13, when the inflow parameter v and the wake skew angle α are appropriately chosen, the 3×3 L-matrix of model no. 6 "shows excellent agreement with prescribed wake results." Model no. 3 is included as a 5×5 analogue of model no. 6,[5,13] both models having uncorrected second and third columns.

Table 1

Elements of M-matrices (Diagonal)

Element	Corrected	Uncorrected
m_{11}	$\frac{128}{75\pi} = .543$	$\frac{8}{3\pi} = .849$
$m_{22} = m_{33}$	$-\frac{256}{945\pi} = -.086$	$-\frac{16}{45\pi} = -.113$
$m_{44} = m_{55}$	$-\frac{256}{1575\pi} = -.052$	$-\frac{256}{1575\pi} = -.052$

Note: For partially-corrected model, use corrected m_{11} and uncorrected m_{22}, m_{33}, m_{44}, m_{55}.

Table 2

Elements of L Matrices

Corrected

5×5 L-matrix for model nos. 1, 2 and 8 & 3×3 L-matrix (partitioned 3×3 matrix) for model nos. 4, 5 and 10

$$\begin{bmatrix} 1/2 & 0 & \frac{525\pi}{2048}\sqrt{\frac{(1-\sin\alpha)}{(1+\sin\alpha)}} & 0 & 0 \\ 0 & \frac{-4}{(1+\sin\alpha)} & 0 & \frac{105\pi}{128}\frac{(1-\sin\alpha)}{(1+\sin\alpha)} & 0 \\ \frac{15\pi}{64}\sqrt{\frac{(1-\sin\alpha)}{(1+\sin\alpha)}} & 0 & -\frac{1}{2}\frac{\sin\alpha(7+\sin\alpha)}{(1+\sin\alpha)} & 0 & 2\sin\alpha(1-\sin\alpha) \\ 0 & -\frac{2205\pi}{2048}\frac{(1-\sin\alpha)}{(1+\sin\alpha)} & 0 & \frac{-\sin\alpha(11-5\sin\alpha)}{(1+\sin\alpha)} & 0 \\ -\frac{3}{7}\frac{(1-\sin\alpha)}{(1+\sin\alpha)} & 0 & -2\sin\alpha(1-\sin\alpha) & 0 & \frac{-6(1+\sin^2\alpha)}{(1+\sin\alpha)^2} \end{bmatrix}$$

Partially Corrected

(Uncorrected second and third columns) 5×5 L-matrix for model nos. 3 and 9 & 3×3 L-matrix (partitioned 3×3 matrix) for model nos. 6 and 11

$$\begin{bmatrix} 1/2 & 0 & \frac{15\pi}{64}\sqrt{\frac{(1-\sin\alpha)}{(1+\sin\alpha)}} & 0 & 0 \\ 0 & \frac{-4}{(1+\sin\alpha)} & 0 & \frac{105\pi}{128}\frac{(1-\sin\alpha)}{(1+\sin\alpha)} & 0 \\ \frac{15\pi}{64}\sqrt{\frac{(1-\sin\alpha)}{(1+\sin\alpha)}} & 0 & \frac{-4\sin\alpha}{1+\sin\alpha} & 0 & 2\sin\alpha(1-\sin\alpha) \\ 0 & -\frac{45\pi}{32}\frac{(1-\sin\alpha)}{(1+\sin\alpha)} & 0 & \frac{-\sin\alpha(11-5\sin\alpha)}{(1+\sin\alpha)} & 0 \\ -\frac{3}{7}\frac{(1-\sin\alpha)}{(1+\sin\alpha)} & 0 & -2\sin\alpha(1-\sin\alpha) & 0 & \frac{-6(1+\sin^2\alpha)}{(1+\sin\alpha)^2} \end{bmatrix}$$

Note: 1. Multiply all elements by 1/v

2. 3×3 L-matrix for model nos. 7 and 12 is given by equation (7) which is partially corrected 3×3 L-matrix with $\alpha = 90°$.

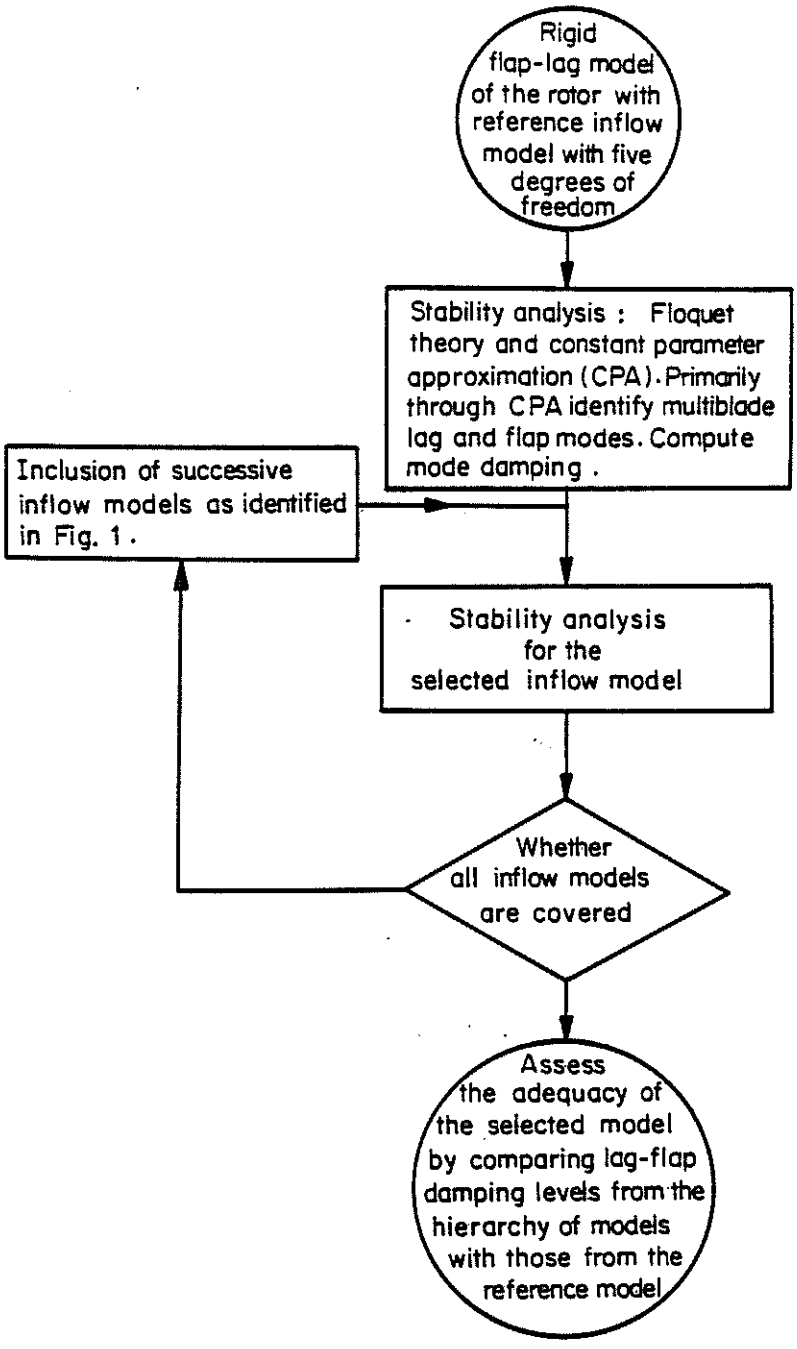

FIG. 2. FLOW CHART FOR ASSESSING THE ADEQUACY OF DIFFERENT DYNAMIC INFLOW MODELS.

3. For model nos. 1 and 2 with five degrees of freedom, the same 5×5 L-matrix from the potential theory is used, whereas the 5×5 M-matrix is based on the corrected lift distributions for model no. 1 and on the uncorrected distributions for model no. 2. A similar pattern is followed for the two 3×3 unsteady models, nos. 4 and 5, in order to assess the effects of apparent mass.

4. All corresponding quasisteady models are included--Nos. 8, 9, 10, 11, 12 and 13. Model no. 13 is the simplest one in that inflow perturbations can be included in the no-inflow models by a simple change of γ to γ^* and C_d to C_d^*.[4]

$$\gamma^* = \frac{\gamma}{(1+a\sigma/8v)} \tag{8}$$

$$(c_d/a)^* = (c_d/a)(1+a\sigma/8v) + (\frac{a\sigma}{8v})(6\,\frac{C_T}{\sigma a})^2 \tag{9}$$

3. Three or More Bladed Rotors with Inflow

We, now, briefly look into the state-variable representation of the rotor and dynamic inflow systems. The rotor system is represented by rigid blades flexibly attached at the rotor centre. The blade executes only rigid flap and lag motions. Individual blade (airfoil) aerodynamics is based on linear, quasisteady theory without the inclusion of stall, compressibility, or other effects due to reversed and radial flow. A rotor schematic is shown in Figure 3 which also includes two coordinate systems -- the rotating system, small (x,y,z); and the non-rotating system, capital (X,Y,Z). By stipulation, the small (x,y,z) system rotates with rotor angular velocity Ω, the period of one rotation being 2π. Therefore, with time unit $1/\Omega$, no distinction need be made between the azimuth angle of the reference blade, ψ_1, and dimensionless time t. The elasticity of the hub (inboard of the blade location where pitch change takes place) is simulated by introducing an elastic coupling or hub rigidity parameter R_h which relates the rotation of the principal axes of the blade-hub system and the blade pitch θ. The spring stiffnesses K_β and K_ζ (Figure 3) are selected such that the uncoupled rotating flap and lag natural frequencies coincide with the corresponding first-mode rotating natural frequencies of the elastic blade. As such, the rotor model is quite adequate to study low-frequency, multiblade instabilities which are highly sensitive to inflow dynamics. The inflow dynamics couple with the blade dynamics as a feedback loop, as outlined in Figure 4.

For convenience, the complete rotor-inflow system is denoted by (X_R, U) where X_R refers to β_k, $\dot{\beta}_k$, ζ_k, and $\dot{\zeta}_k$ of the k-th blade in the rotating frame; and U refers to the inflow components v_o, v_s, v_c, v_{2s}, and v_{2c} in the non-rotating frame. When multiblade coordinates are used (non-rotating frame) X_R is replaced by Y. For a three-bladed rotor, X_R represents (β_k, $\dot{\beta}_k$, ζ_k, $\dot{\zeta}_k$) for k varying from 1 to 3; and Y represents (β_o, $\dot{\beta}_o$, β_c, $\dot{\beta}_c$, β_s, $\dot{\beta}_s$, ζ_o, $\dot{\zeta}_o$, ζ_c, $\dot{\zeta}_c$, ζ_s, $\dot{\zeta}_s$). Thus, for a rotor system with N blades and for an inflow system with five degrees of freedom, the rotor-inflow system has the state variable representation:

$$\dot{X}_R = [A(t)]_{4N\times 4N}\, X_R + [N(t)]_{4N\times 5}\, U \tag{10a}$$

The dynamics of the inflow system, as typified by equation (6), can be expressed as

$$M\,\dot{U} + L^{-1}\,U = F(t)\,X_R + G(t)\,U$$

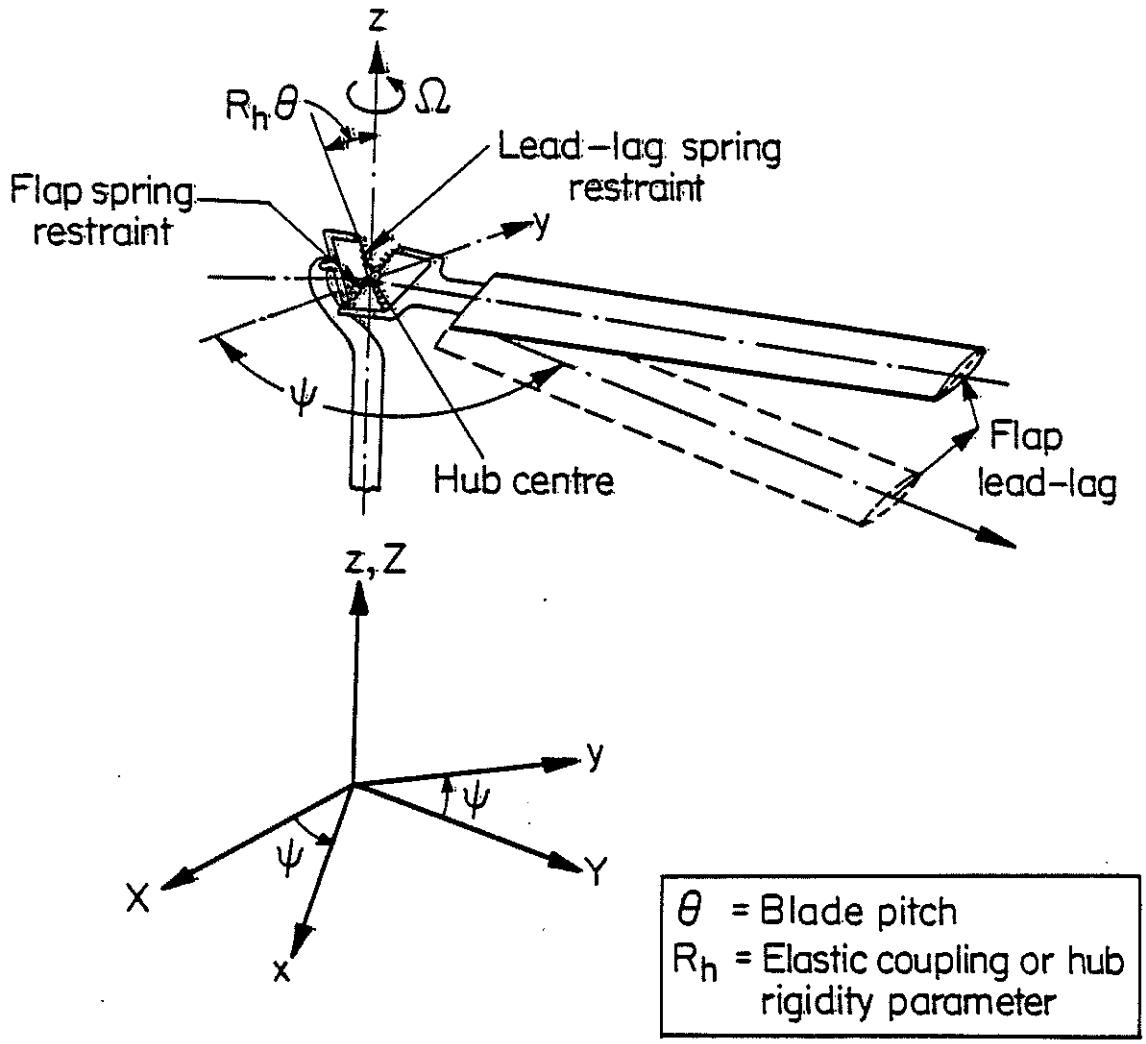

FIG. 3. ROTOR SCHEMATIC

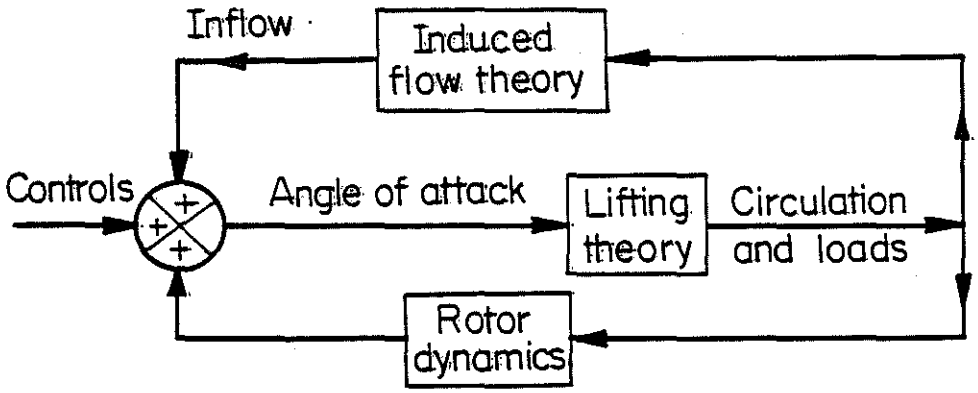

FIG. 4. BLOCK DIAGRAM OF INFLOW DYNAMICS.

which reduces to

$$\dot{U} = [-M^{-1} L^{-1} + M^{-1} G] U + M^{-1} F X_R \tag{10b}$$

If B(t) represents the 4N×4N multiblade coordinate-transformation matrix,[8] we have

$$X_R = B(t) Y \tag{10c}$$

The state equation for the rotor-inflow system can then be expressed as

$$\begin{Bmatrix} \dot{Y} \\ \dot{U} \end{Bmatrix}_{(4N+5)\times 1} = \begin{bmatrix} B^{-1} A B - B^{-1}\dot{B} & B^{-1} N \\ M^{-1} F B & -M^{-1}L^{-1}+M^{-1} G \end{bmatrix} \begin{Bmatrix} Y \\ U \end{Bmatrix}_{(4N+5)\times 1} \tag{10d}$$

In the quasisteady formulation, the second row of equation (10d) simplifies to

$$U = [[I - L G]^{-1} L F B] Y \tag{11}$$

Consequently, equation (10d) takes the form

$$\dot{Y} = [B^{-1} A B - B^{-1}\dot{B} + B^{-1}N [I-L G]^{-1} L F B] Y_{(4N\times 1)} \tag{12}$$

Basically, a study of a rotor system with unsteady inflow reduces to the treatment of equation (10d) which involves matrices A, B, $\dot{B}$, B^{-1}, N, M, M^{-1}, F, G and L. For the rigid flap-lag rotor model, (A, B, $\dot{B}$, B^{-1}) are generated as in reference 8. The matrix N(t) is given in Table 3. Observe that the elements of N(t) pertaining to ν_o, ν_s, and ν_c agree with those of earlier studies[4,6-8] in which an inflow model with three degrees of freedom from momentum theory is used. The remaining two matrices--F and G--refer to the air loads C_T, C_L, C_M, C_{2L}, and C_{2M}. They are too cumbersome to reproduce here.

When the inflow model is either momentum theory or the 3×3 potential theory, and when the rotor has 3 or more blades, equation (12) represents a constant-parameter system for $\mu = 0$. Furthermore, the periodic terms are not large (even for $0 < \mu < .3$) due to the multi-blade representation. However, when the inflow model is the 5×5 potential theory (which implies the addition of second-harmonics of loads and inflow), then the equations have strong periodic coefficients even for $\mu = 0$. Although these periodic terms initially surprised us; in retrospect, they should have been expected. They are, in fact, somewhat analogous to the periodic terms that occur at $\mu = 0$ when the 3×3 inflow model (first-harmonics of loads and inflow) is applied to a rotor with less than 3 blades. In the latter case, the 3×3 model requires instantaneous thrust, roll moment, and pitch moment; but a two-bladed rotor has roll and pitch moments with large 2/rev oscillations due to the lack of polar symmetry. In a similar manner, the 5×5 model requires instantaneous thrust, roll moment, pitch moment, second-harmonic roll, and second-harmonic pitch. For a three-bladed rotor, however, only three of these vary smoothly with time. The second-harmonic components of blade loading vary erratically yielding periodic coefficients. Another way of looking at this problem is as a result of trying to represent a continuous lift distribution by discrete blade loadings. For a three-bladed rotor, at any point in time, the "continuous" loading implicit in potential (actuator-disc) theory is represented

Table 3

Elements of $N(t_k)$

$$\frac{\gamma}{8}\begin{bmatrix} 0 & 0 & 0 & 0 & 0 \\ -(\frac{4}{3}+2\mu St) & -(1+\frac{4}{3}\mu St)St & -(1+\frac{4}{3}\mu St)Ct & -(\frac{4}{5}\mu St)S2t & -(\frac{4}{5}+\mu St)C2t \\ 0 & 0 & 0 & 0 & 0 \\ *\begin{cases} +3\phi+4\mu\bar{\beta}Ct & (2\phi+\frac{8}{3}\mu\bar{\beta}Ct)St & (2\bar{\phi}+\frac{8}{3}\mu\bar{\beta}Ct)Ct & (\frac{3}{2}\phi+2\mu\bar{\beta}Ct) & (\frac{3}{2}\bar{\phi}+2\mu\bar{\beta}Ct)C2t \\ -\bar{\theta}(\frac{4}{3}+2\mu St) & -\bar{\theta}(1+\frac{4}{3}\mu St)St & -\bar{\theta}(1+\frac{4}{3}\mu St)Ct & -\bar{\theta}(\frac{4}{5}+\mu St)S2t & -\bar{\theta}(\frac{4}{5}+\mu St)C2t \end{cases} \end{bmatrix}$$

$St = \sin t_k$; $Ct = \cos t_k$, $k=1,2,\ldots,N$

*4th row

by only 3 discrete points on $0 < \psi \leq 2\pi$. These three points can be used to uniquely define C_T, C_L, and C_M (as in a finite Fourier series); but one cannot expect to consistently define five loadings from only three points. We suspect, however, that a five-bladed rotor with the 5×5 potential theory would provide a consistent model having constant coefficients at $\mu = 0$.

4. Numerical Results

The damping data given below are generated for the moment-trimmed condition ($\bar{f} = \bar{\beta}_s = \bar{\beta}_c = 0$) typical of main rotors as in reference 4. Base-line and additional parameters are identified in Table 4. The details of the ordering scheme are identical to those of references 4 and 8. The manually derived rotor-inflow state equations have been found to agree with the computer-generated ones for the ordering scheme $1 >> \varepsilon^2$, where ε is a small quantity of the order of β_k, $\bar{\lambda}$, $\bar{\theta}_k$, $\sqrt{c_d/a}$ etc., for details see reference 15.

While computing the 'L' matrices given in Table 3, we have identified the incidence angle α with the wake skew angle downstream of the rotor such that

$$\alpha = \tan^{-1} [(\bar{\lambda}+\bar{v})/\mu] \tag{13}$$

When α_s represents the shaft angle of attack, we have (with small angle assumption): $\bar{\lambda} = \alpha_s\mu + \bar{v}$ for $\bar{f} \neq 0$, and $\bar{\lambda} = \bar{v}$ for $\bar{f} = 0$. We should note, however, that Reference 5 suggests that the wake skew angle at the rotor be used in [L],

$$\alpha \text{ [at rotor]} = \tan^{-1} [\bar{\lambda}/\mu] \tag{14}$$

and the value at the rotor seems to give good correlation with a prescribed wake theory.[13] The downstream α (rather than α at the rotor) was inadvertently used here, but the resultant damping values are little changed by this difference. Figure 5 provides a plot of α downstream for two values of $\bar{f}$ as well as a plot of α at the rotor for $\bar{f} = 0$. Other parameters pertinent to the figure are $C_T/\sigma = .2$, $\sigma = .05$, $a = 2\pi$. The results show that the difference in the values of α should not affect the conclusions to be drawn.

In the results to follow, damping curves are labelled as regressing, collective, or progressing modes. When identifying frequencies in this manner in a Floquet analysis, a degree of subjectivity cannot be avoided. As a matter of fact, one could get all the three multiblade inplane or flapping modes practically for the same frequency value due to frequency ambivalence inherent in the Floquet analysis.[16] In the present study, multiblade modes have been more precisely identified with the help of the constant-parameter approximation (CPA) for an advance ratio range of $0 \leq \mu \leq 0.4$. In CPA, there is less ambiguity concerning these frequencies, though such an approach is not always foolproof, particularly for $\mu > 0.25$ or so.[8] Such an identification has also been found to be consistent with the eigenvector analyses of FTMS[16] and with the physics of the problem in that the lowest-frequency lag regressing mode is usually the most affected by dynamic inflow. On the other hand, we realize that, for $\mu > .25$, modes may be significantly coupled; and the terms "collective, etc." may have diminished physical meaning.

Unless stated otherwise, all the subsequent numerical results in Figure 6 to 12 refer to the base-line configuration identified in Table 4. In data presentation, the low-frequency ($\omega \approx 0.3$) lag regressing mode is emphasized, since it is most affected by inflow. It is also the crucial mode in several flight dynamics problems.[1,7] Data for the collective and progressing modes ($\omega \approx 0.7, 1.7$) are also presented, however, for completeness.

Table 4

Rotor-Inflow System Parameters for Numerical Results

Parameters	Base Line Values	Additional Values
μ	0.35	Variable (0 - 0.4)
γ	5	-----
Elastic Coupling (R_h)	Nil (0)	-----
P	1.15	-----
ω_ζ	0.7	1.4
C_T/σ	0.2	Variable (0.05 - 0.30)
σ	0.05	----
N	3	-----
C_d/a	$0.01/2\pi$	-----
Equilibrium Condition	Moment Trimmed ($\bar{f} = 0.0$)	-----
α	From Equation (13) (see Figure no. 5)	0 (edgewise flow)

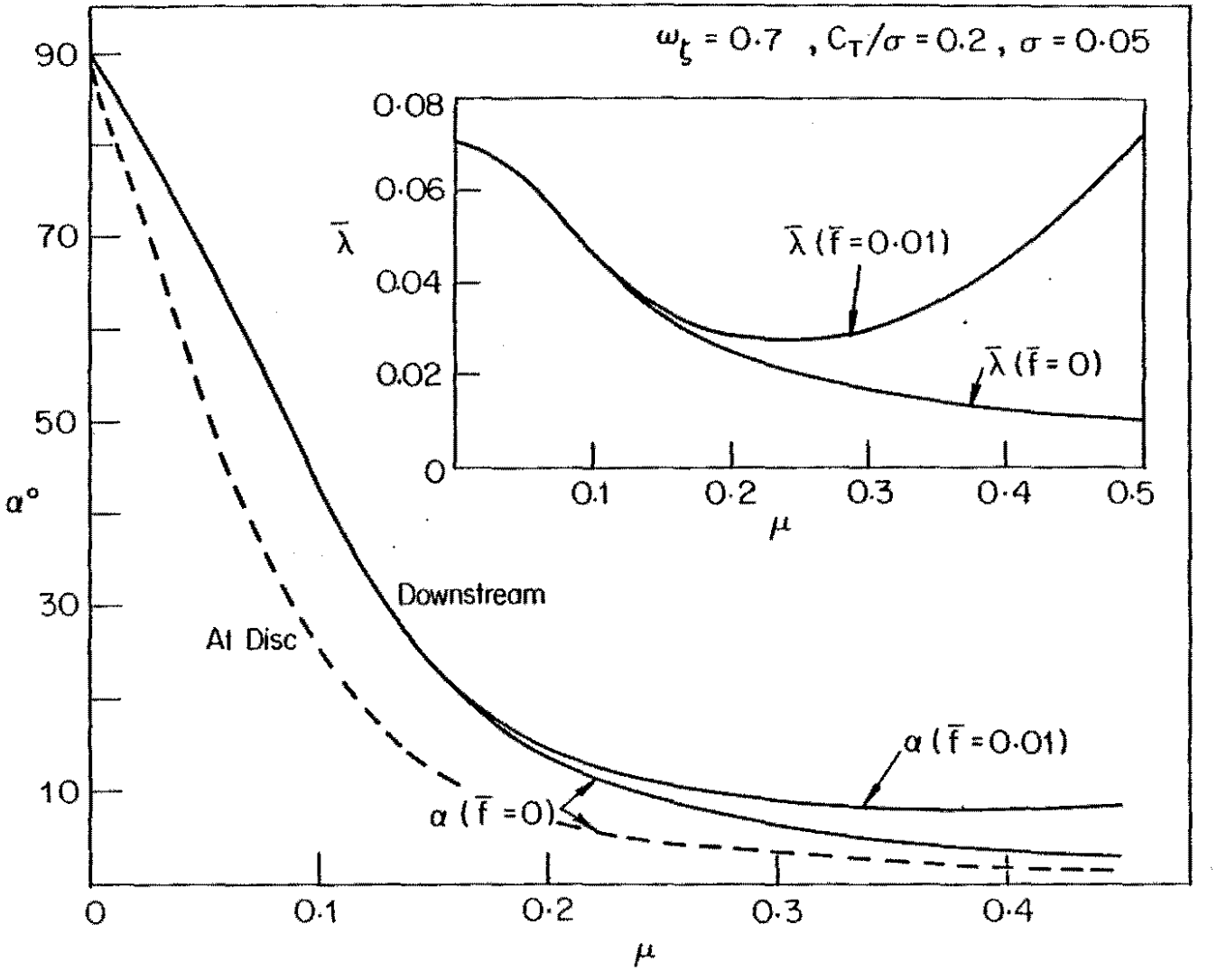

FIG. 5 . STEADY INFLOW AND DISK ANGLE OF ATTACK AS A FUNCTION OF ADVANCE RATIO.

We begin with Figure 6 which gives the lag damping of the regressing mode for each inflow model. First, let us consider the region of high advance ratio. For large μ ($.25 < \mu < .4$), we know from previous work[2] that the dynamic inflow is virtually quasi-steady; and this is born out by the fact that differences in apparent mass among models 1-3 (or among models 4-6) have virtually no effect on damping. The high-μ data further show that, in this quasi-steady regime (in which the L matrix dominates), there is little effect of the details of lift distribution (corrected versus partially corrected). In other words, models 2 and 3 agree as do models 5 and 6. The high-μ data also show that there is a marked difference in damping levels between the 3×3 potential theories (4-8) and the 5×5 potential theories (1-3). The 18% change in damping between the 3×3 and 5×5 models (at high μ) was not expected, and is difficult to rationalize physically. We will, however, return to this phenomenon shortly, after studying more results.

In the low-μ region of Figure 6 ($0 < \mu < .15$), both quasi-steady and unsteady terms are important. A comparison of models 1-6 shows that the M_{11} term has negligible effect on regressing damping (2 and 3 have the same damping, 5 and 6 the same) whereas the M_{22} and M_{33} terms have a strong effect (1 differs from 2-3, 4 differs from 5-6). This is to be expected due to the decoupling of collective modes (including ν_o, M_{11}) in hover. Also in the low-μ region, we note that both momentum theory (7) and the 3×3 models with uncorrected second and third columns (5,6) give nearly identical results. This is to be expected since these potential-flow models reduce to momentum theory in the limit as $\mu \to 0$. What is surprising, however, is the agreement between momentum theory (7) and the 3×3 potential models (4-6) as μ becomes large. The maximum error in the <u>effect</u> of inflow is 20%, and the maximum error in <u>total</u> damping is about 10%. This agreement occurs despite large qualitative differences among the [L] matrices at large μ. We hasten to add, however, the test data on forced response has previously shown large differences between results with momentum theory and results with more sophisticated [L] matrices.[2] Therefore, we may not conclude from this one figure that momentum theory is always adequate. A comparison of 3×3 potential flow models to 5×5 models at low μ (i.e. compare 1 and 4, 2 and 5, or 3 and 6) shows only 11% difference as compared to 18% difference at high μ. From this, we conclude that it is the fourth and fifth rows and columns of [L] that cause the major discrepancies. The M_{44} and M_{55} terms, on the other hand, seem to alleviate the differences. This further implies that the higher-frequency variations in C_{2L} and C_{2M}, which tend to dominate the quasi-steady results at high μ, are somewhat filtered out by the apparent mass terms, which come into play at low μ.

Finally, we note that, despite the various differences among the results, all dynamic inflow theories give qualitatively similar results; and all theories show large deviations (over 50%) with respect to the theory without inflow for the damping of the regressing mode.

A similar plot for the damping of the collective mode is given in Figure 7. Here, in contrast to Figure 6, the M_{11} term is seen to have the major effect at low μ. (Note that the M_{11} of model 2 differs from that of models 1, 3; and M_{11} of model 5 differs from that of 4, 6.) The sensitivity to M_{11} is to be expected because M_{11} represents the apparent mass of ν_o which should dominate the ζ_o (collective) mode. It is interesting for the collective mode that there is little difference between the damping from the 3×3 and 5×5 inflow models (1 agrees with 4, 2 with 5, and 3 with 6). Again, this is to be expected since the 2/rev variation in induced flow (introduced in the 5×5 model) should have no average effect on a uniform (i.e. collective) mode at low μ. On an overall basis, the agreement among 1,3,4,6 and also between 2,5 are a consequence of the decoupling of the collective mode at low μ. Figure 8 provides the third plot, that of the progressing mode, to complete the set of damping curves. The low-μ values show similar trends to

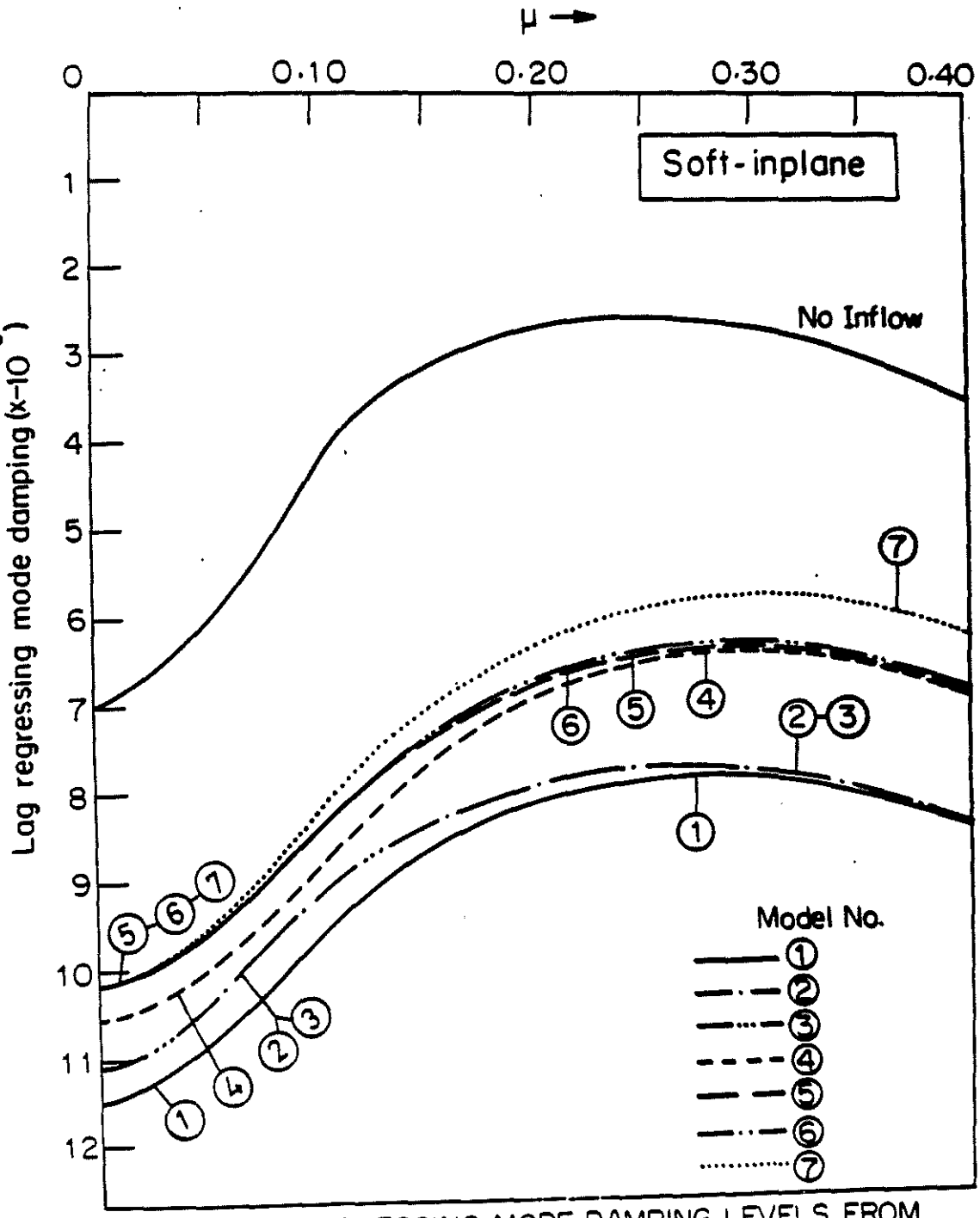

FIG. 6 : LAG REGRESSING MODE DAMPING LEVELS FROM SEVEN UNSTEADY INFLOW MODELS.

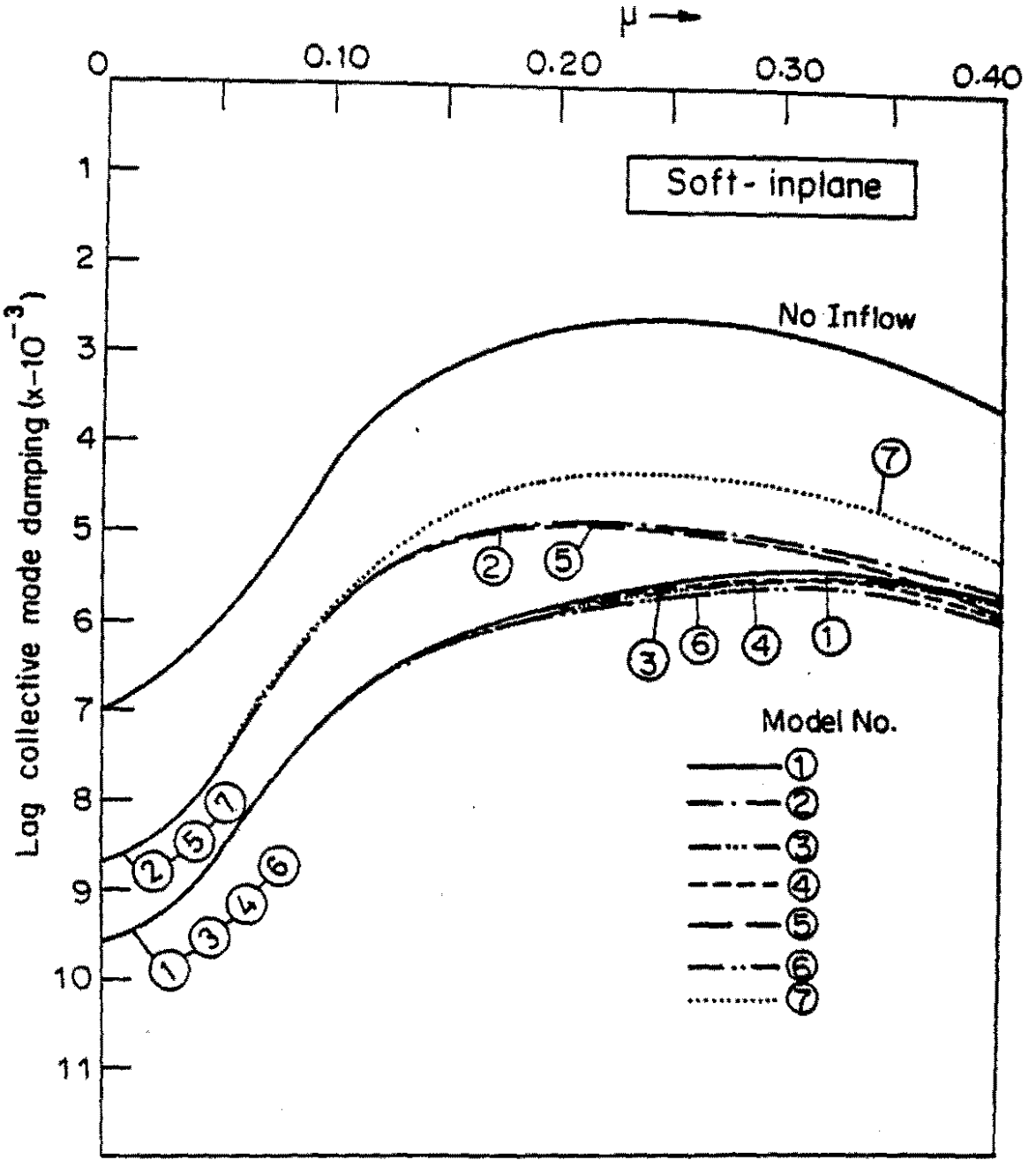

FIG. 7: LAG COLLECTIVE MODE DAMPING LEVELS FROM SEVEN UNSTEADY INFLOW MODELS.

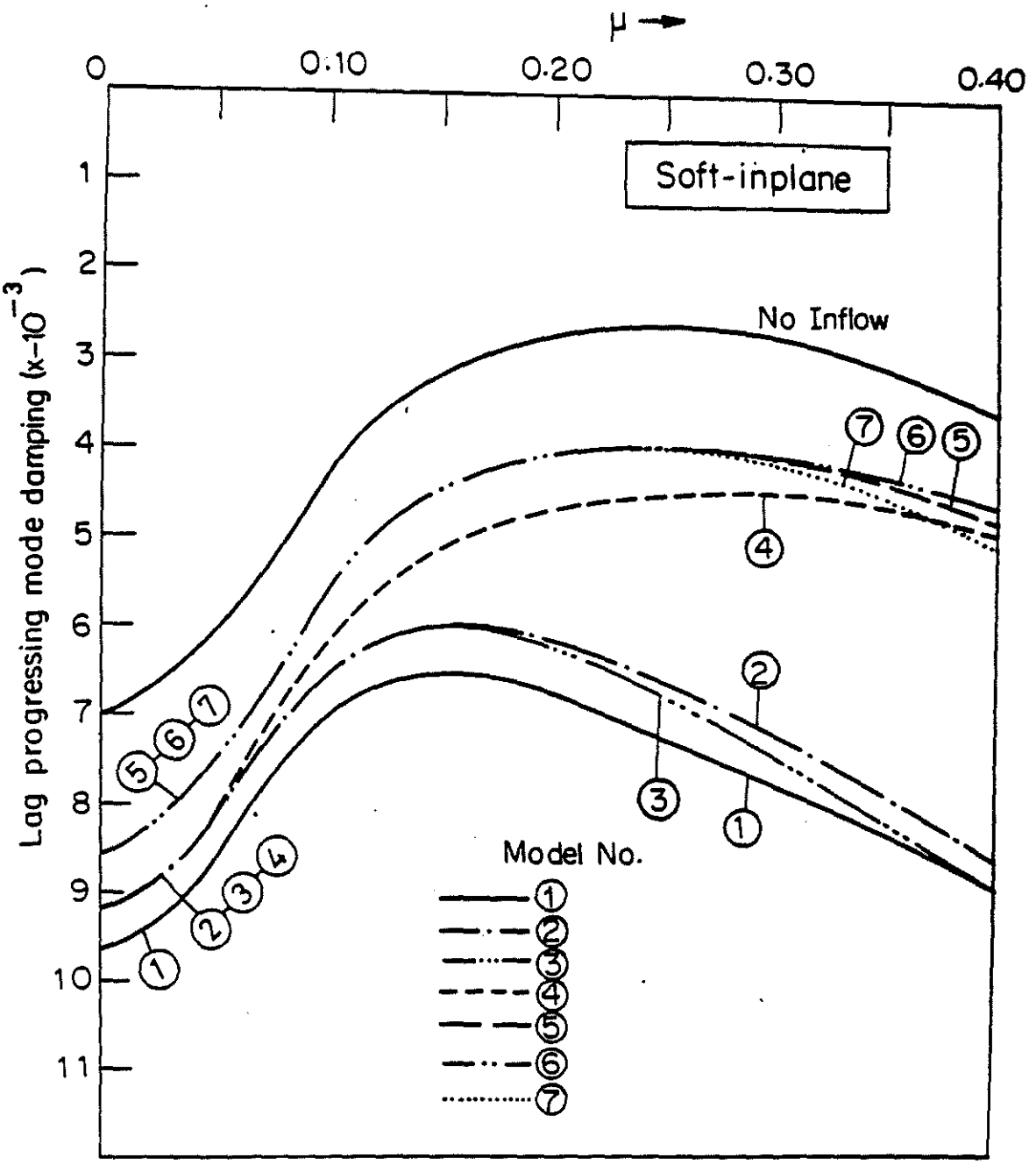

FIG. 8 : LAG PROGRESSING MODE DAMPING LEVELS FROM SEVEN UNSTEADY INFLOW MODELS.

those of Figure 6 due to the fact that M_{22} and M_{33} provide the major influence on damping. We also comment that the agreement between 2 and 4 seems a numerical coincidence, and it does not occur on other plots. The high-μ portion of the curves is also similar to that of Figure 6 with two marked differences: 1) the discrepancy between the 3×3 and 5×5 models is much larger for the progressing mode than for the regressing mode; and 2) the 5×5 results do not approach the NO-INFLOW theory as μ becomes large. These two observations place serious doubts upon the consistency of the 5×5 model, as discussed below.

We recall the earlier discussion concerning the use of three discrete blade loadings to replace the continuous disc-loading implied by potential theory. In that discussion, we stated that this approximation could result in extraneous, large oscillation in C_{2L} and C_{2M} (and thus in ν_{2s} and ν_{2c}). The results in Figures 6 and 8 indicate that indeed this is happening. These extraneous oscillations contaminate the low-frequency, regressing mode to account for 18% error; and they contaminate the high-frequency, progressing mode by a much greater amount (100%). Further justification for this conclusion is to be found in the results of the constant-parameter approximation, not shown here. For those results, periodic coefficients (including the extraneous periodicity at $\mu = 0$ in the 5×5 model) are neglected. The results indicate a much closer agreement between 3×3 and 5×5 models than is found in Figure 6, and many of the damping curves are virtually identical with the two models. This points to the fact that it is periodicity, not the fourth and fifth columns, that give the differences between 3×3 and 5×5 models. We therefore believe that the 5×5 model should not be used for rotors with fewer than 5 blades. Further calculations must be done to verify whether or not 5-bladed rotors will have these problems. Meanwhile, since most conventional rotors have four blades or less, we recommend abandonment of the 5×5 models and use only of the 3×3 models.

The following figures deal with further verification of the conclusions in Figures 6-8. Figure 9 shows damping results with the six quasi-steady inflow models. The data, when compared to that of Figure 6, show that the high-μ results of that earlier figure are indeed quasi-steady. Figure 9 also shows, in agreement with Figures 6-8, that momentum theory captures the major effects of inflow on lag damping. This is seen in the agreement between momentum theory and the 3×3, partially-corrected model. In fact, all 3×3 models (10, 11, and 12) are very close in Figure 9. Another interesting aspect of Figure 9 is the agreement among quasi-steady models 10-13 (3×3 models) and among quasi-steady models 8-9 (5×5 models) at $\mu = 0$. This is in contrast to marked differences in their unsteady counterparts, Figure 6. The conclusion is clear. At low μ, it is entirely the effect of apparent mass (not changes in [L]) that creates differences among the 3×3 (or among 5×5) models. On the other hand, differences between the 3×3 group (10-12) and the 5×5 group (8-9) persist at $\mu = 0$, which indicates the [L] matrix and periodicity as the source of those differences.

Figure 10 pursues the effect of thrust coefficient on the regressing damping at $\mu = 0.35$. The data show that the conclusions reached earlier are independent of rotor lift, although the differences among theories do increase slightly with C_T/σ. In particular, the maximum error is 13% for $C_T/\sigma = 0.1$, 16% for $C_T/\sigma = .15$, and 18% for $C_T/\sigma = .20$. Figure 11 repeats regressing damping but for zero angle of incidence. Although $\alpha = 0$ is not strictly possible for $\mu \equiv 0$, α can remain zero as μ approaches zero, with proper choice of shaft angle and rotor speed. Since $\alpha = 0$ gives the maximum possible deviation between momentum theory and potential theory, Figure 11 gives an upper bound on this deviation for a rotor with $\omega_\zeta = 0.7$. Perhaps the most meaningful comparison in the figure is that between momentum theory (7) and the partially corrected 3×3 model (6). At low μ, the zero angle of incidence

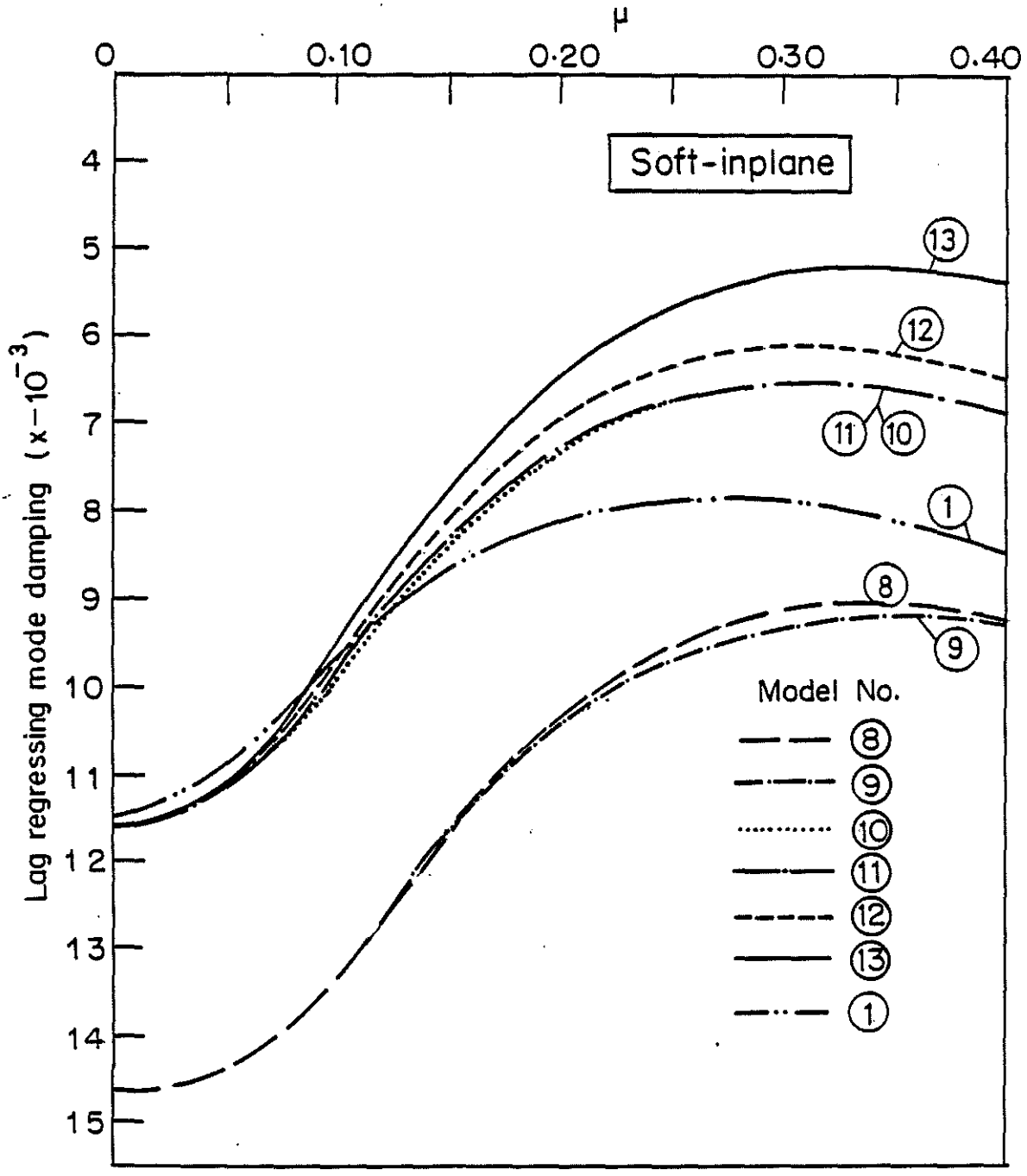

Fig. 9. LAG REGRESSING MODE DAMPING FROM SIX QUASISTEADY MODELS.

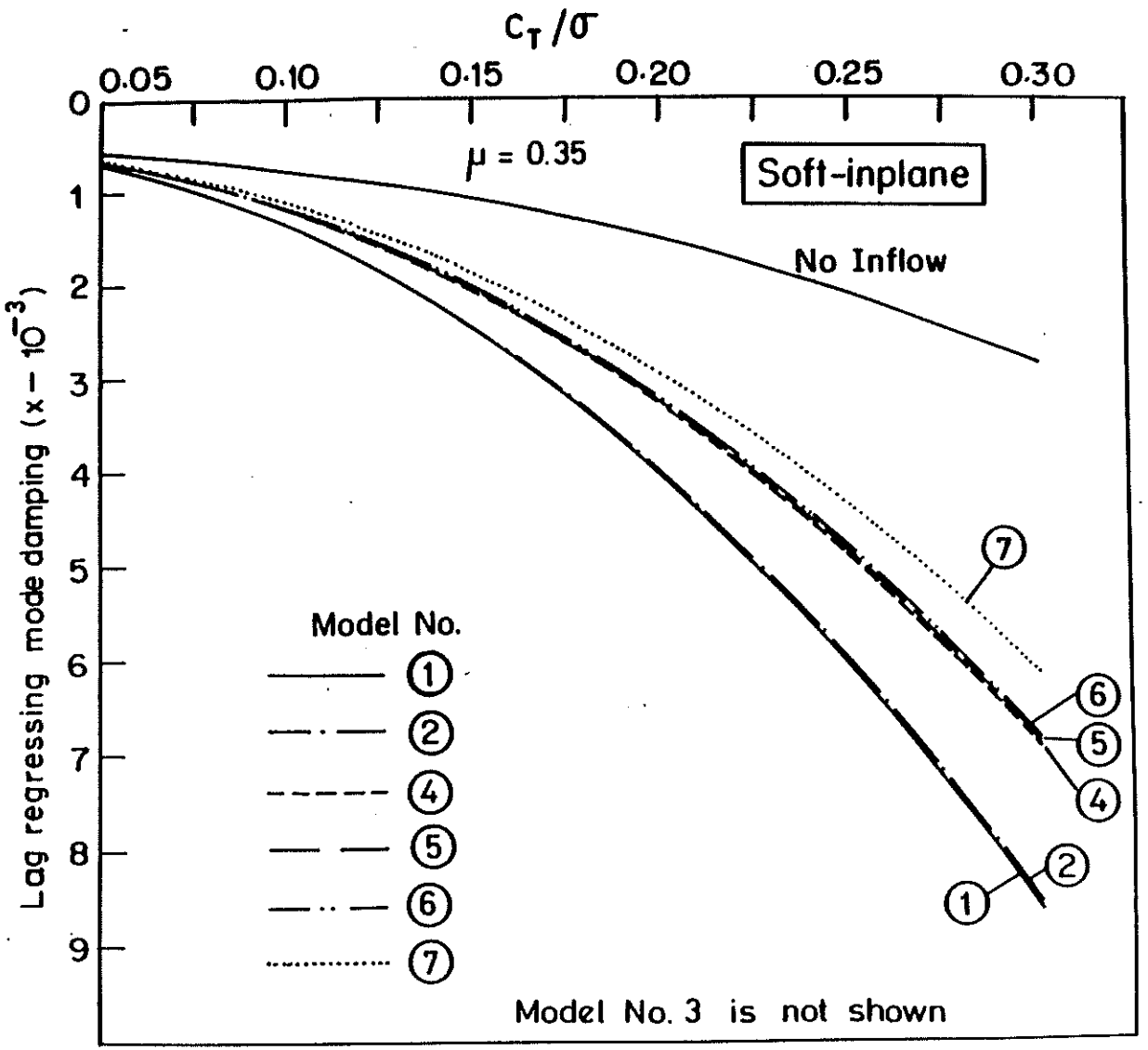

Fig. 10. LAG REGRESSING MODE DAMPING AS A FUNCTION OF C_T/σ

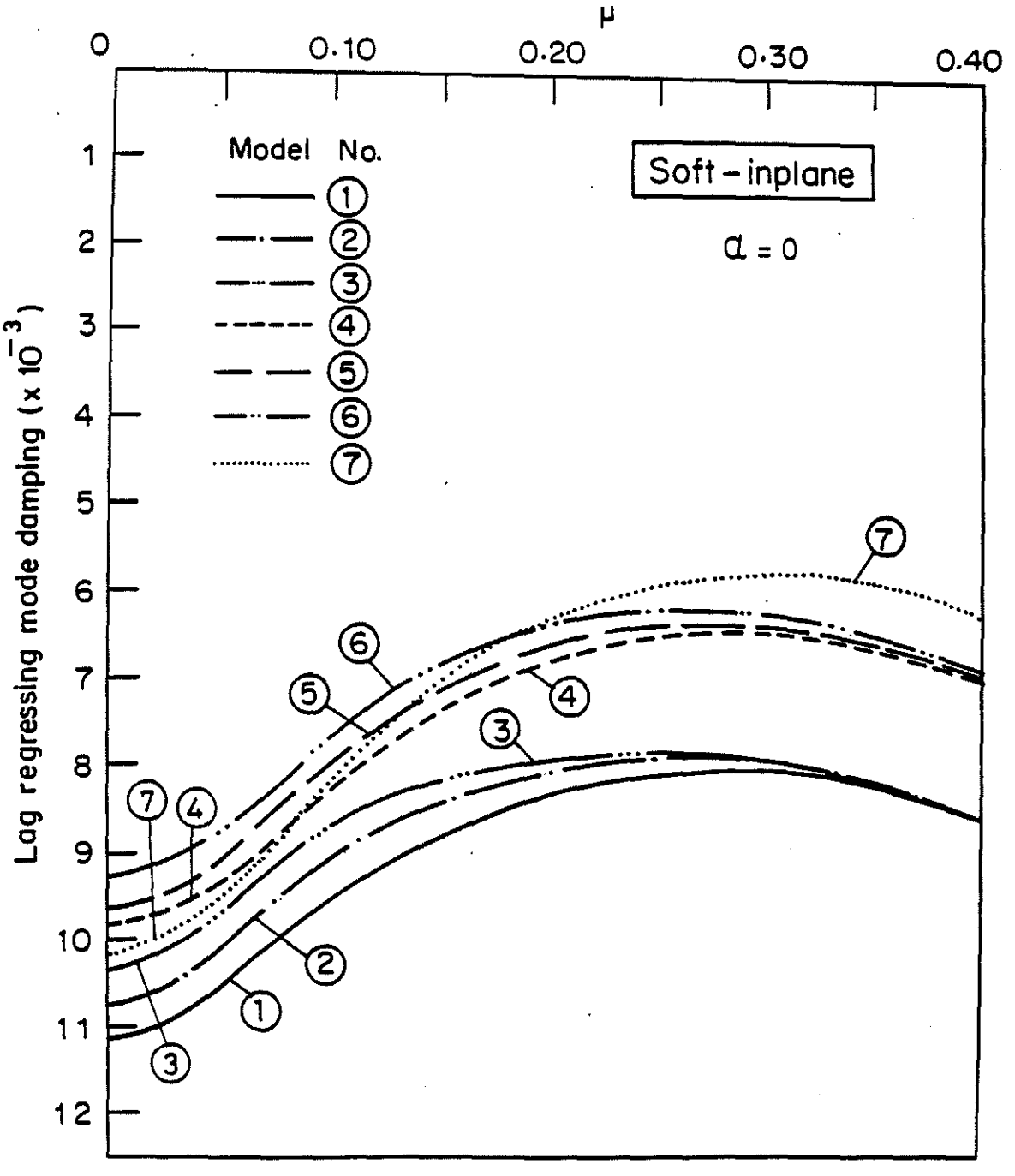

Fig. 11. LAG REGRESSING MODE DAMPING FROM SEVEN UNSTEADY MODELS FOR EDGEWISE FLOW.

draws curve 6 away from curve 7 and closer to the no-inflow results ($\eta = 7\times10^{-3}$ at $\mu = 0$). The difference is a significant percentage of the total effect of inflow. Therefore, we conclude that, under appropriate conditions, there can be a large difference between the results with momentum theory and the results with the 3×3 potential theory. Finally, Figure 12 presents damping data for the regressing mode of a stiff inplane rotor, $\omega_\zeta = 1.4$. All of the conclusion of Figure 6 (soft inplane rotor) are verified with one deviation. The momentum theory results (for damping) show poorer agreement with the 3×3 potential model in Figure 12 than they do in Figure 6 (50% of inflow effect versus 20%). Thus, momentum theory is not adequate for this particular configuration.

Other results (not shown here) show that all unsteady dynamic inflow models give nearly identical results for flap damping. Thus flap-damping is not sensitive to dynamic inflow model, although flap forced response is sensitive to the model.

5. Conclusions

The following conclusions are based on a rigid-blade, flap-lag model of a 3-bladed rotor with fixed hub. Therefore, these conclusions must be tempered by the fact that they apply only to this model and with respect to the accuracy of the flap and inplane damping. With that in mind, we draw the following conclusions.

1. The 5×5 inflow model should be abandoned since it leads to an inconsistent rotor-wake model for rotors with less than 5 blades.

2. The 3×3, partially-corrected inflow model remains the clear choice for a simple, accurate description of dynamic inflow.

3. For some choices of system parameters, the flap-lag damping with the 3×3 model is very close to the damping with the momentum-theory model; but for other parameter sets, momentum theory can be in error by as much as 50% with respect to the effect of dynamic inflow.

4. The greatly simplified γ^*-C_d^* approximation, although not giving an accurate quantitative measure of the effect of inflow, nevertheless is qualitatively accurate for trend studies throughout the entire parameter range.

5. At high advance ratio, the effect of inflow is primarily quasi-steady and is insensitive to the particular lift distribution upon which [L] is based.

6. At low advance ratios, apparent mass terms play a major role in the flap-lag damping; but the differences in [M] between corrected and uncorrected lift distributions account for only a 5%-10% change in damping.

7. Necessary future work includes application of the inflow models to 2-bladed and 5-bladed rotors, as well as use of the 3×3 partially-corrected model in calculations of flapping response.

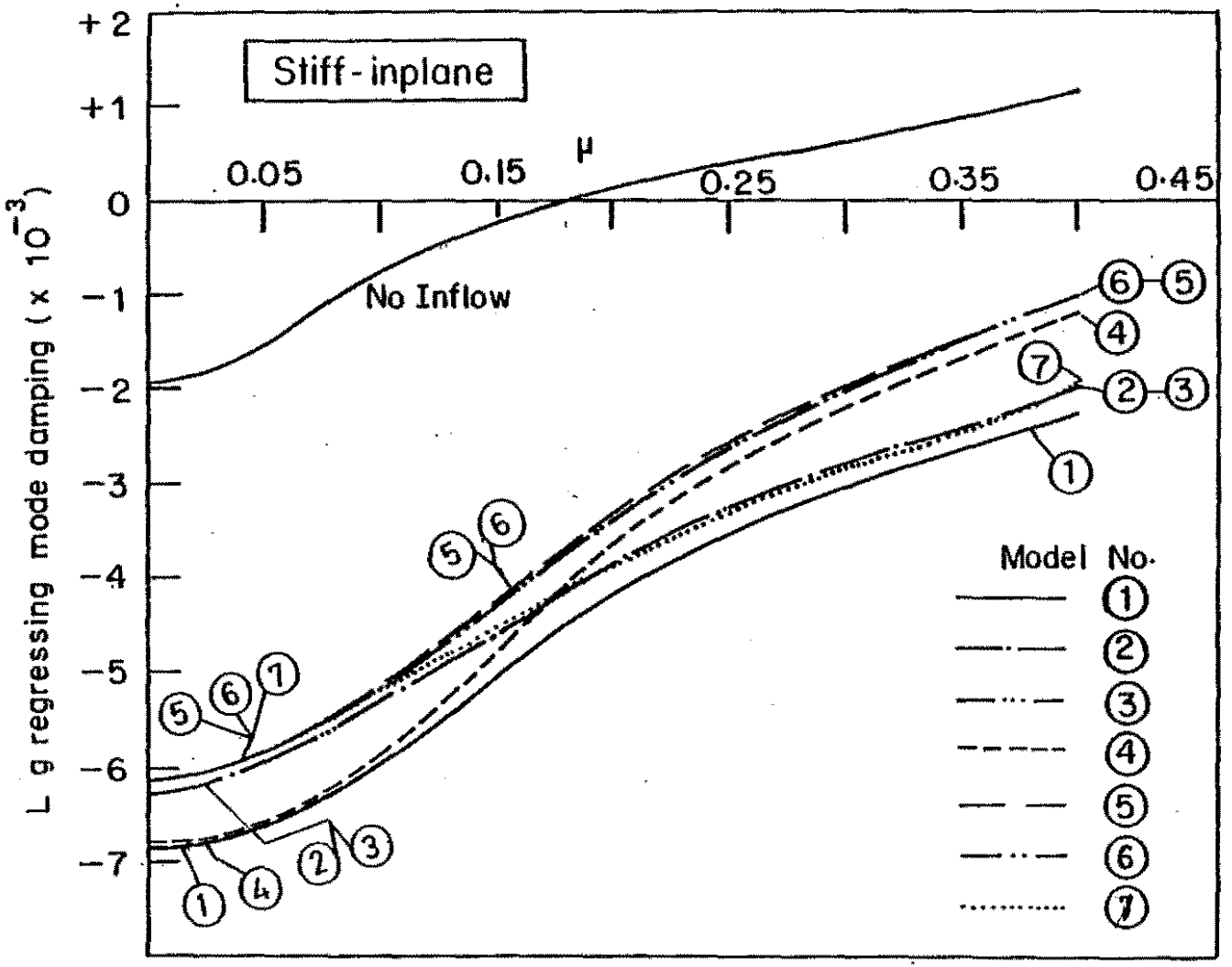

Fig. 12. LAG REGRESSING MODE DAMPING FOR A STIFF INPLANE ROTOR FROM SEVEN UNSTEADY MODELS.

6. References

1. K.H. Hohenemser, "Flight Dynamics of Hingeless Rotorcraft", AGARDOgraph, No. 197, September 1974, pp. 28-29.

2. D.A. Peters, "Hingeless Rotor Frequency Response with Unsteady Inflow", Rotorcraft Dynamics, NASA-SP-352, February 1974, pp. 1-12.

3. R.A. Ormiston, "Application of Simplified Inflow Models to Rotorcraft Dynamic Analysis," Journal of the American Helicopter Society, Vol. 21, July 1976, pp. 34-37.

4. D.A. Peters and G.H. Gaonkar, "Theoretical Flap-lag Damping with Various Dynamic Inflow Models," Journal of the American Helicopter Society, Vol. 25, No. 3, July 1980, pp. 29-36.

5. D.M. Pitt and D.A. Peters, "Theoretical Prediction of Dynamic-Inflow Derivatives", Sixth European Rotorcraft and Powered Lift Aircraft Forum, Bristol, England, Paper No. 47, September 1980; Vertica, Vol. 5, No. 1, Jan. 1981.

6. G.H. Gaonkar, A.K. Mitra, and D.A. Peters, "Feasibility of a Rotor Flight-Dynamics Model with First Order Cyclic Inflow and Multiblade Modes," AIAA Dynamics Specialists Conference, Atlanta, April 1981, AIAA Paper No. 81-0611-CP.

7. G.H. Gaonkar, A.K. Mitra, T.S.R.Reddy, and D.A. Peters, "Sensitivity of Helicopter Aeromechanical Stability to Dynamic Inflow", VERTICA, The International Journal of Rotorcraft & Powered Lift Aircraft, Vol. 6, No. 1, 1982, pp. 59-75.

8. G.H. Gaonkar and D.A. Peters, "Use of Multiblade Coordinates for Helicopter Flap-Lag Stability with Dynamic Inflow", Journal of Aircraft, Vol. 17, No. 2, Feb. 1980, pp. 112-119.

9. K.H. Hohenemser and S.T. Crews, "Model Tests on Unsteady Rotor Wake Effects", Journal of Aircraft, Vol. 10, No. 1, January 1978, pp. 58-60.

10. D. Banerjee, S.T. Crews, K.H. Hohenemser, and S.K. Yin, "Identification of State Variables and Dynamic Inflow from Rotor Model Dynamic Tests", Journal of the American Helicopter Society, April 1977, Vol. 22, No. 2, pp. 28-36.

11. D. Banerjee, S.T. Crews, K.H. Hohenemser, and S.K. Yin, "Parameter Identification Applied to Analytic Hingeless Rotor Modeling", Journal of the American Helicopter Society, Vol. 24, No. 1, January 1979, pp. 26-32.

12. R.A. Ormiston, "An Actuator Disk Theory for Rotor Wake Induced Velocities", AGARD-CP-111, Fluid Dynamics Specialists Meeting, Marseilles, France, September 13-15, 1972.

13. D.M. Pitt, "Rotor Dynamic Inflow Derivatives and Time Constants from Various Inflow Models", USATSARCOM-TR81-2, December 1980.

14. K.W. Mangler and H.B. Squire, "The induced velocity field of a rotor", Aeronatucial Research Council Reports & Memoranda, No. 2642, May 1950.

15. J. Nagabhushanam, G.H. Gaonkar, and T.S.R. Reddy, "Automatic Generation of Equations for Rotor-Body Systems with Dynamic Inflow for a Priori Ordering Schemes", Seventh European Rotorcraft and Powered Lift Aircraft Forum, Garmisch-Partenkirchen, Germany, September 1981, Paper No. 37.

16. G.H. Gaonkar, D.S. Simha Prasad, and D. Sastry, "On Computing Floquet Transition Matrices of Rotorcraft", Paper No. 45, Fifth European Rotorcraft and Powered Lift Aircraft Forum, September 4-7, 1979, Amsterdam, The Netherlands; The Journal of the American Helicopter Society, Vol. 26, No. 3, July 1981, pp. 29-36.

7. Acknowledgement

The authors are grateful to the late Professor A.R.S. Bramwell for his assistance in developing closed-form expressions for the [L] matrix. We would also like to thank Mr. J. Nagabhushanam for his hard work and persistence in writing and executing the computer programs.

Dr. Peters' contribution to this research was sponsored by the National Science Foundation, NSF Grant No. CME-7906304.